CRYSTAL GROWTH & DESIGN

pubs.acs.org/crystal Article

Probing the Kinetics of Crystallite Growth in Sol−Gel Derived Metal-Oxides Using Nanocalorimetry

Andre Zeumault* and Steven K. Volkman

Cite This: *Cryst. Growth Des.* 2020, 20, 1590−1597 Read Online

ACCESS | Metrics & More | Article Recommendations | Supporting Information

ABSTRACT: In this work, we show that fast-scanning chip nanocalorimetry can be used to kinetically separate the heat flow contributions of crystallite growth and precursor decomposition that occur during the thermal decomposition of metal-oxide solgel precursors. We illustrate the technique using zinc acetate dihydrate, a common precursor used in the sol-gel synthesis of zinc oxide thin films. Through an appropriately defined heating sequence consisting of precursor decomposition, followed by rapid quenching and subsequent zinc oxide crystallite growth, it is shown that the exothermic peaks corresponding to the growth of zinc oxide crystals can be kinetically separated from the endothermic peaks associated with precursor decomposition. The kinetic separation of these processes enables an analysis to be performed on the crystallite growth kinetics of zinc oxide within a zinc acetate matrix, as it would naturally occur during a solgel process. Through a quantitative analysis, we estimate the activation energy of crystallite growth, confirming Johnson−Mehl−Avrami growth kinetics at low heating rates, and extract a time−temperature-transformation diagram to visualize and quantify isocrystalline surfaces. Such fundamental knowledge regarding the evolution of crystallinity as a function of heating conditions is useful in the much broader sense of application development, serving as a guide to direct the precise thermokinetic engineering of crystallinity in sol−gel derived metal-oxide films. In particular, we emphasize its significance for electronic (ideally, high crystallinity), optoelectronic, and thermoelectric (ideally, low crystallinity) applications.

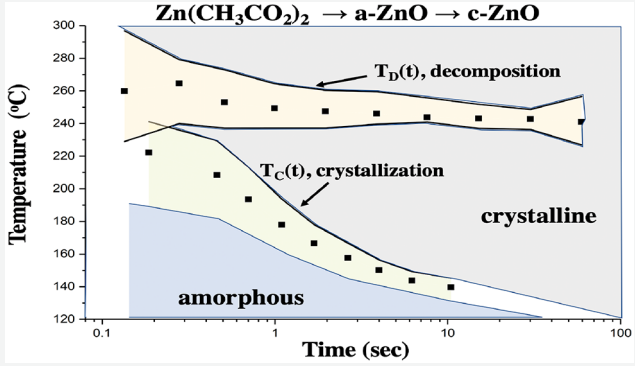

INTRODUCTION

The development of solution-processed, high-performance metal-oxides films has the potential to enable new technology based upon cost-effective, digitally fabricated,[1−3] flexible and transparent electronics,[4] optoelectronics,[5] and thermoelectrics.[6] In order to meet the needs of these applications and expand the versatility of these materials even further, the development of synthetic methods that allow the control of film crystallinity (analogous to physical vapor deposited films[7]) from fully amorphous to fully crystalline is desired, since crystallinity and film structure have a direct influence upon materials properties of interest, including electronic and thermal transport, defect electrostatics,[8] and optical transparency.[9]

To date, metal-oxide films synthesized from sol−gel methods[10−12] greatly outperform films obtained from nanoparticle suspensions,[13] both in terms of carrier transport and lower processing temperatures.[14] Despite these advantages, unfortunately, controlling crystallinity in sol−gel metal-oxide films is difficult due to large heat of formation,[15] small activation energy of crystallization,[16−18] and high decomposition temperatures of sol−gel precursors.[19,20] Consequently, crystallization of the metal-oxide product and chemical decomposition of the sol−gel precursor are coupled by temperature, resulting in metal-oxide films which tend to be either nanocrystalline and fully converted into the metal-oxide[21−24] or semicrystalline and partially converted into the metal-oxide[25] as-deposited.

This lack of synthetic control over composition and crystallinity in metal-oxide films synthesized from sol−gels was first addressed using conventional calorimetry by Rupp and coworkers.[26] In their work, they've extended the use of time−temperature-transformation (TTT) diagrams, historically used in processing glasses[27] and steel,[28] to monitor the crystallization thermokinetics of metal-oxide thin-films through conventional differential scanning calorimetry (DSC). Their work elucidates the oft-used solute-drag effect in suppressing the crystallinity of alloyed metal-oxide films[29,30] through a retardation of growth rates but does not address the coupled nature of chemical decomposition and crystallization leading to the initial formation of mixed amorphous/crystalline phases during the chemical conversion into the oxide phase. As evidenced in their work, as-deposited "amorphous" CeO_2 and gadolinium alloyed $Ce_{0.8}Gd_{0.2}O_{1.9-x}$ films had similar crystallite sizes of 7 and 8 nm

Received: October 9, 2019
Revised: January 31, 2020
Published: February 7, 2020

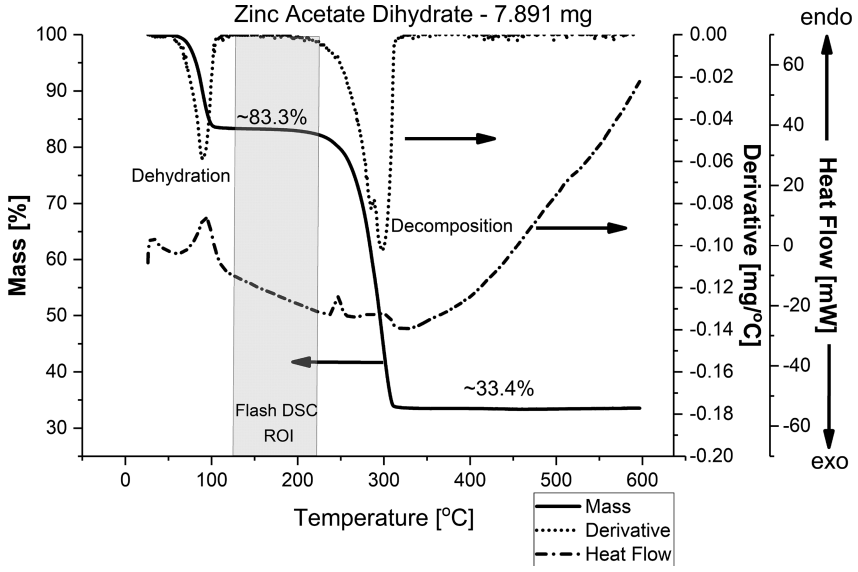

Figure 1. Thermogravimetric analysis of zinc acetate dihydrate powder collected at a heating rate of 10 °C min^{-1} under 20 mL min^{-1} dry N_2.

respectively, albeit a small crystalline fraction.[26] Thus, apart from the apparent uncertainty regarding the definition of the amorphous to mixed amorphous+crystalline phase boundary in a TTT diagram, more importantly, the utility of the solute-drag effect is ultimately limited by the initial crystallization processes occurring during oxide formation before solute solubility in the host lattice becomes relevant (i.e., solute drag). To extend existing efforts to synthetically define crystallinity in sol−gel derived metal-oxide films using TTT diagrams, it is advantageous to explore the initial growth of metal-oxide domains immediately following the chemical decomposition (and metal-oxide nucleation) of the sol−gel precursor. We will show that such information is appropriately accessed using an in situ kinetic separation technique via fast scanning chip nanocalorimetry.

In this work, we utilize the high heating and cooling rates of flash DSC to kinetically separate the otherwise parallel processes of chemical decomposition and crystallite growth occurring during the thermal decomposition of metal-oxide sol−gel precursors. To illustrate the methodology using a simple, well-known system, we studied zinc oxide synthesized from the thermal decomposition of zinc acetate dihydrate, a common sol−gel precursor. Owing to the ubiquity of zinc acetate dihydrate as a sol−gel precursor for zinc oxide formation, the mechanism of the thermal decomposition of zinc acetate dihydrate into zinc oxide has been studied in great detail and can be used to supplement our thermokinetic analysis. A temperature profile (Figure 2) was defined based upon thermogravimetric analysis (TGA) shown in Figure 1, intended to perform the following sequence:

(1) Decompose the sol−gel precursor and nucleate the metal-oxide product.

(2) Quench thermal energy to prevent subsequent growth of the oxide product during the decomposition/nucleation process.

(3) Grow the as-formed nuclei at variable rates to assess crystallite growth kinetics.

After application of this temperature sequence, we observed distinct exothermic transformations occurring well below the precursor decomposition temperature determined by conventional TGA/DSC, suggesting crystallite growth. Applying a kinetic model analysis to these exothermic peaks, we obtain results consistent with the well-known Johnson−Mehl−Avrami (JMA) model of crystal growth as the heating rate is reduced logarithmically from 100 °C s^{-1} to 1 °C s^{-1}. Thus, this work provides a direct method to study the rapid growth kinetics of metal-oxides in situ proceeding from the thermal decomposition of their sol−gel precursors and within a dynamic environment consisting of the sol−gel precursor and metal-oxide species as it occurs during typical sol−gel synthesis.

Moreover, the association of the kinetically separated exothermic peaks with a crystallite growth process provides thermokinetic information specifically related to the precursor chemistry and is used to define a TTT diagram having precise crystallinity in addition to a more reliable amorphous/crystalline phase boundary. These phase diagrams define the temperatures and heating rates leading to crystallite growth and may thus serve as a guide for the improved control of thin-film crystallinity for electronic applications—favoring high crystallinity—as well as thermoelectric or optoelectronic applications—favoring low crystallinity.

EXPERIMENTAL SECTION

Materials. Zinc acetate dihydrate powder (Sigma-Aldrich, 379786) was used as-received, without further preparation, in all of the subsequent thermal analysis methods.

TGA/DSC. For TGA/DSC measurements, 7.891 mg of as-received zinc acetate dihydrate powder was loaded into a 70 μL alumina crucible having an alumina lid (Mettler-Toledo, 24123). The equipment used to perform the measurement was a Mettler-Toledo TGA/DSC 3+. The heating rate used was 10 °C min^{-1}, and the flow gas was ultrahigh purity 5.0 grade nitrogen (Airgas, UHP300) at a flow rate of 20 mL min^{-1}. The Mettler-Toledo Star^e evaluation software was used to compute derivatives of the mass, including onset and endset temperatures, as well as changes in mass loss associated with dehydration and decomposition.

Flash DSC. For flash DSC measurements, a single particle of zinc acetate dihydrate, having immeasurably small mass (<1 μg) was carefully placed onto the center of the sample area of a flash DSC chip sensor (Mettler-Toledo, 51192133). To load the sample, a single bristle of a paint brush was used that had been dipped in silicone oil to facilitate transfer of the powder to the sample area of the chip sensor. Silicone oil is commonly used for this purpose of transferring, as it does not

https://dx.doi.org/10.1021/acs.cgd.9b01339
Cryst. Growth Des. 2020, 20, 1590−1597

undergo thermal transformations within the range of temperatures explored by the flash DSC and can be viewed as a spectator. The equipment we used to perform the measurement was a Mettler-Toledo Flash DSC 1. The equipment capability, sample loading effects, and calibration details have been described in detail for the Flash DSC 1 elsewhere.[31]

Data Analysis. Numerical routines for data analysis and visualization were implemented using the Python programming language (version 2.7.12). Background fitting, applied to the measured heat-flow, was performed using an asymmetric least-squares smoothing algorithm assuming positive peaks with appropriate fitting parameters ($\lambda = 10^{10}$, $p = 10^{-6}$).[32]

RESULTS AND DISCUSSION

Conventional TGA/DSC Produces Indistinct Transformations. In this section, we discuss the inadequacy of conventional TGA/DSC to separately quantify heat flow contributions from chemical decomposition and that due to crystallite growth in metal-oxide sol−gel precursors. Additionally, we discuss the development of a temperature profile suitable for flash DSC analysis, which allows decomposition and crystallization to be separated kinetically.

The result of applying a TGA/DSC to zinc acetate dihydrate powder at a typical heating rate of 10 °C min^{-1} is shown in Figure 1. The mass percentage is plotted along the primary axis at the left, while the derivative (DTA) and heat flow (DSC) are plotted on the secondary axes shown at the right. As shown, there are two distinct regions at low and high temperatures where significant mass loss occurs. The onset and endset temperatures of the lower temperature peak are 77 and 99 °C respectively, whereas the onset and endset temperatures of the higher temperature peak are 237 and 293 °C respectively, as determined from the derivative of the mass percentage. These results are consistent with other reports that have associated the lower temperature peak with dehydration of zinc acetate dihydrate into zinc acetate and the higher temperature peak with decomposition of the zinc acetate into zinc oxide via melting and sublimation of the acetate.[33]

For our purposes, we highlight the observation that the DSC signal shown in Figure 1 indicates that the endothermic peaks associated with decomposition (between 250 and 300 °C) and the broad exothermic peak (between 300 and 350 °C) associated with the crystallization process cannot be distinctly separated. This overlap in temperature leads to an ambiguous quantification of the heat flow associated with the respective processes in these regions. Further analysis requires kinetic separation of the two processes utilizing the high heating/cooling rates available via flash DSC.

To ensure kinetic separation in what follows, a region of interest is selected, between 125 and 225 °C, in which no decomposition or thermal transformations occur under conventional slow heating rates (i.e. thermodynamic conditions). Thus, by applying an appropriate heating sequence defined to decompose the sol−gel precursor and rapidly quench the temperature prior to crystallite growth 2, exothermic transitions observed within this region of interest upon subsequent heating are most likely due to the growth of zinc oxide crystals which nucleated during the thermal decomposition of the zinc acetate, as will be shown in the following sections through kinetic model analysis.

Kinetic Separation of Thermal Transformations via Flash DSC. Having demonstrated the inadequacy of conventional heating rates in separating the heat-flow contributions from chemical decomposition and crystallite growth, in this section we discuss the results of applying flash DSC to zinc acetate dihydrate powder within the region of interest highlighted in Figure 1 (i.e., 125−225 °C) to kinetically separate the two processes.

The TGA data in Figure 1 were used to develop a suitable temperature profile for flash DSC shown in Figure 2. As

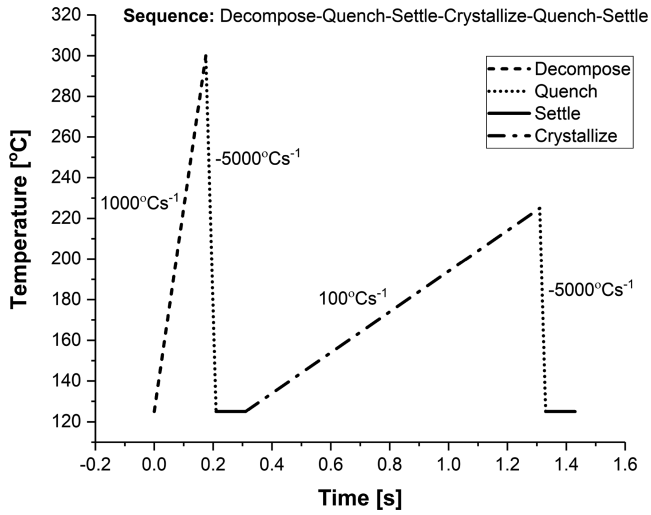

Figure 2. Heating profile applied to zinc acetate dihydrate powder for flash DSC measurements.

intended, first the sample is dehydrated by heating to 125 °C at 10 °C min^{-1}, and subsequently held at 125 °C for 2 min. Next, a sequence of two heating and cooling cycles is applied to first decompose and subsequently crystallize the sample, respectively. Since decomposition of zinc acetate leads to nucleation of zinc oxide, to ensure that the nucleation time does not vary for each heating cycle, the heating rate used in the decomposition heating cycle was fixed at 1000 °C s^{-1}. The use of higher heating rates during decomposition is favorable as it reduces unwanted crystallite growth immediately following nucleation. However, higher heating rates also shift phase transitions toward higher temperatures in which the rate of crystallite growth is higher. To balance these concerns, a heating rate of 1000 °C s^{-1} was selected to ensure the decomposition temperature was observable up to a maximum temperature of 300 °C, only 7 °C higher than the endset decomposition temperature determined from conventional TGA/DSC at 10 °C min^{-1}. To prevent further crystallite growth upon cooling, the sample is rapidly quenched at −5000 °C s^{-1} immediately following each heating cycle. Here, an instantaneous quench is desired to prevent crystallite growth immediately following nucleation. However, a maximum cooling rate of 5000 °C s^{-1} was used as it corresponds to the maximum cooling rate accessible to the standard flash DSC calorimeter chips throughout the entire operating temperature range without nonlinear rate variation as determined elsewhere.[31] For the second heating cycle, intended to crystallize the sample, the heating rate is varied logarithmically from 100 °C s^{-1} to 1 °C s^{-1}. This is the primary variable in the experiment, the heating rate, and is used to assess the kinetics of crystallite growth. An example heating profile is shown in Figure 2 for a heating rate of 100 °C s^{-1}. This profile is repeatedly applied with the same parameters to the same sample except with a different heating rate.

The application of a sequence of heating profiles having different heating rates (example in Figure 2) to zinc acetate

https://dx.doi.org/10.1021/acs.cgd.9b01339
Cryst. Growth Des. 2020, 20, 1590−1597

dihydrate powder produced distinct exothermic and endothermic transformations as shown in Figure 3. The measured heat flow corresponding to the entire temperature profile is given in Supporting Information Figure S1. Here, the heat flow associated with only the heating cycles is shown. As shown, the exothermic transformation is a strong function of the heating rate as expected for a crystallite growth process. Similarly, apart from the initial thermal cycle (100 °C s^{-1}), the endothermic transformation is roughly invariant between thermal cycles, as intended.

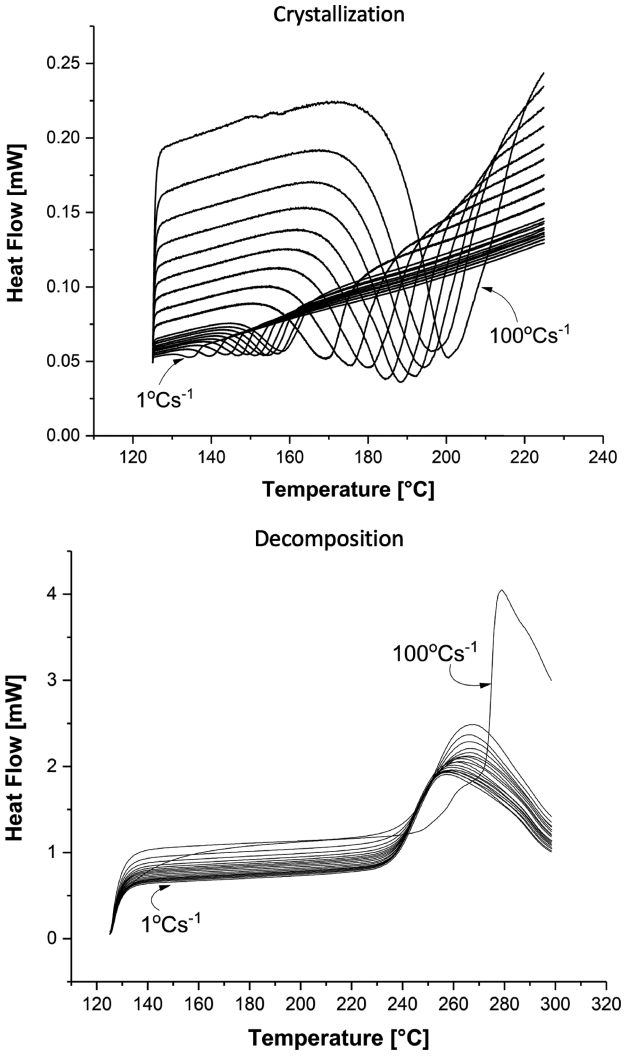

Figure 3. (Top) Heat flow versus sample temperature for the exothermic peaks associated with crystallite growth. (Bottom) Heat flow versus sample temperature for the endothermic peaks associated with decomposition.

We note that each exothermic transformation necessarily follows a decomposition step as shown in the Supporting Information Figure S2. Furthermore, repeated measurements of the same heating profile yield approximately the same result as shown in Figure S3. These observations suggest a controlled sequential process of decomposition and crystallization achieved via rapid heating and quenching between heating cycles. Thus, the kinetics associated with the exothermic peaks corresponds to the growth of zinc oxide crystals from as-formed zinc oxide nuclei and can be reliably quantified through the application of a kinetic model analysis for the exothermic peaks as discussed in the following section.

Kinetic Model Analysis of Exothermic Peaks. In this section, we discuss the results of applying a kinetic model analysis to the exothermic peaks shown in Figure 3 to gain physical insight into the crystallite growth process, obtain rate information, and produce the raw data necessary to define a TTT diagram. Details regarding the method used here for assessing non-isothermal crystallization kinetics have been reported elsewhere.[34] Here, we show only what is necessary to interpret the main analytical results.

The heat flow ϕ and extent of conversion α are shown with respect to the sample temperature in Figure 4 and Figure 5

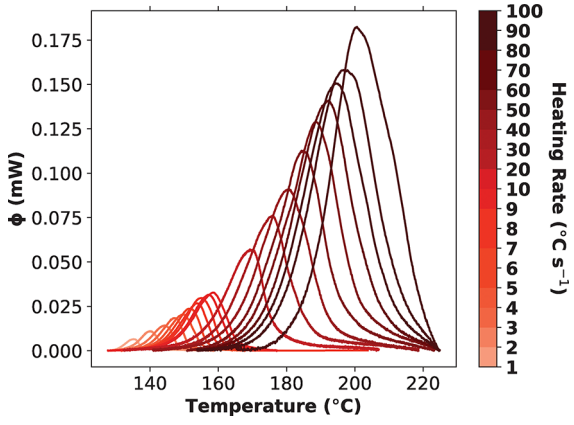

Figure 4. Heat flow versus sample temperature. The baseline for each curve was obtained by applying an asymmetric least-squares fitting algorithm of the peaks and subtracted accordingly.[32] Each curve corresponds to a different heating rate, varied from 100 °C s^{-1} to 1 °C s^{-1}.

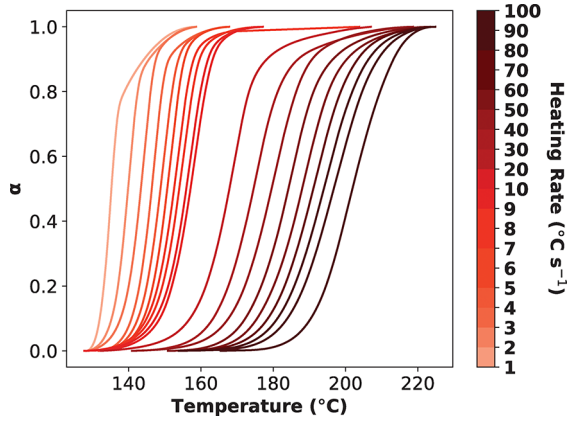

Figure 5. Extent of conversion versus sample temperature obtained from integration and normalization of heat-flow data shown in Figure 4. Each curve corresponds to a different heating rate, varied logarithmically from 100 °C s^{-1} to 1 °C s^{-1}.

respectively as a family of curves corresponding to the different heating rates varied logarithmically from 100 °C s^{-1} to 1 °C s^{-1}. For convenience, here we have plotted as positive the values of heat flow for exothermic transformations. For the heat flow, which serves as the raw input for the subsequent kinetic analysis, the baseline was fit by applying an asymmetric least-squares fitting algorithm of the peaks and subtracted accordingly.[32]

According to Figure 4, as the heating rate is reduced from 100 °C s^{-1} to 1 °C s^{-1}, the entire transformation shifts monotonically

https://dx.doi.org/10.1021/acs.cgd.9b01339
Cryst. Growth Des. 2020, 20, 1590−1597

toward lower temperatures. Since the transformations occur at higher temperatures for higher heating rates, this implies that the rate of transformation, being thermally activated, is higher at higher heating rates. Furthermore, the measured heat flow has the expected dependence upon the heating rate, namely, that the measured heat flow ϕ is proportional to the product of the heating rate β, the enthalpy of conversion ΔH, and the nonisothermal rate of conversion $\frac{d\alpha}{dT}$ and therefore reduces as the heating rate is reduced (eq 1).

$$\frac{d\alpha}{dT} = \frac{1}{\beta}\frac{\phi}{\Delta H} \tag{1}$$

Information regarding the rate of conversion can be obtained by extracting the activation energy associated with this process using the measured heat-flow ϕ and the sample temperature and is independent of the kinetic model function[35,36] according to eq 2.

$$\left[\frac{d(\ln(\phi))}{d(1/T)}\right]_{\alpha} = -\frac{E_A}{R} \tag{2}$$

According to Figure 6, at low heating rates (1−10 °C s^{-1}) the average activation energy is 97.70 kJ mol^{-1} and is constant with respect to the extent of conversion α from 0.30 to 0.70. By contrast, we note that at higher heating rates (10−100 °C s^{-1}), the activation energy was 63.96 kJ mol^{-1} on average, but was dependent upon the extent of conversion from 0.30 to 0.70. The reduction in activation energy with extent of conversion may indicate a surface-mediated growth process that becomes relevant at higher heating rates. For comparison, the activation energy was also determined using the Ozawa (90.06 kJ mol^{-1}, see Figure S4) and the Kissinger methods (83.73 kJ mol^{-1}, see Figure S5) and is consistent with the activation energy evaluated at lower heating rates. We note that these values are similar to the values reported for the activation energy of crystallization of metal-oxides and glasses thought to exhibit the same growth kinetics.[16−18]

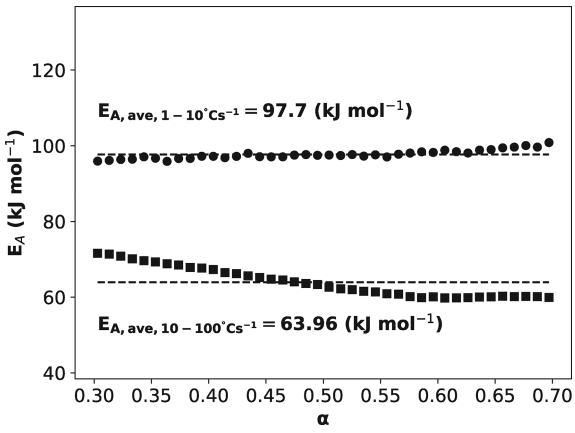

Figure 6. Activation energy extracted from Arrhenius plot of the extent of conversion.

An Avrami plot is shown in Figure 7, showing clear linear trends for all rates. For crystallization processes, linearity of the Avrami plot is often used to validate the Johnson−Mehl−Avrami (JMA) model, though practical concerns have been raised due to the insensitivity of a double-logarithmic function to its argument.[37] A more reliable test is performed using the kinetic model functions $y(\alpha)$ and $z(\alpha)$ (eq 3 and eq 4).[34]

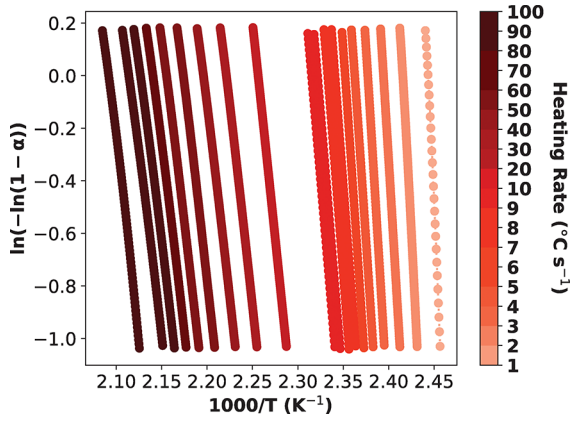

Figure 7. Avrami plot used to test the validity of the JMA model.

$$y(\alpha) = \phi e^{E_A/RT} \tag{3}$$

$$z(\alpha) = \phi T^2 \tag{4}$$

The kinetic model functions $y(\alpha)$ and $z(\alpha)$ are presented in Figure 8. For the JMA model to be valid, the maxima of $z(\alpha)$, denoted α_z*, should be roughly 0.632 ± 0.02. As a visual aid, we've plotted this region of JMA validity as a dashed vertical box, as has been done elsewhere.[34] As the heating rate is reduced, α_z* approaches the region of JMA validity. This can be seen more

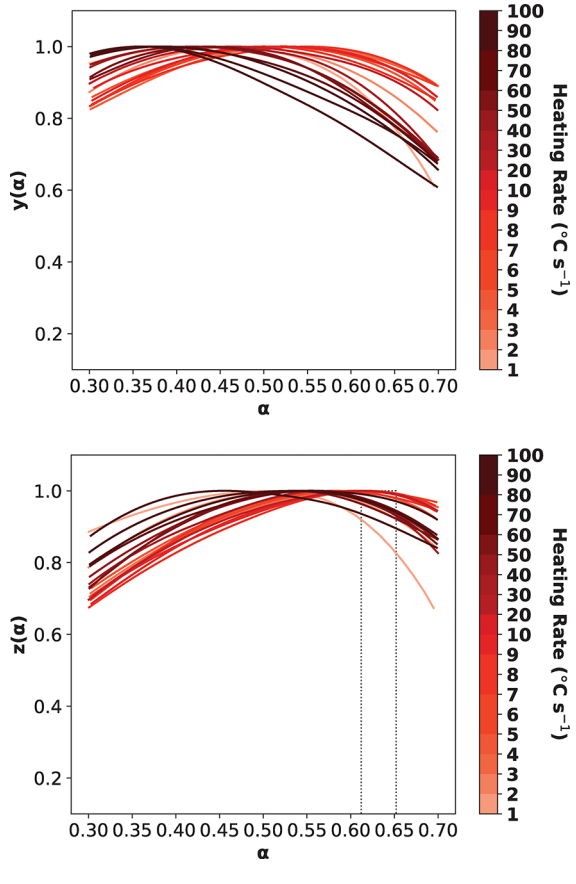

Figure 8. Normalized kinetic model function (top) $y(\alpha)$ and (bottom) $z(\alpha)$.

https://dx.doi.org/10.1021/acs.cgd.9b01339
Cryst. Growth Des. 2020, 20, 1590−1597

clearly in Figure 9, where α_y* and α_z*, the maxima of the respective functions, have been plotted explicitly for the various

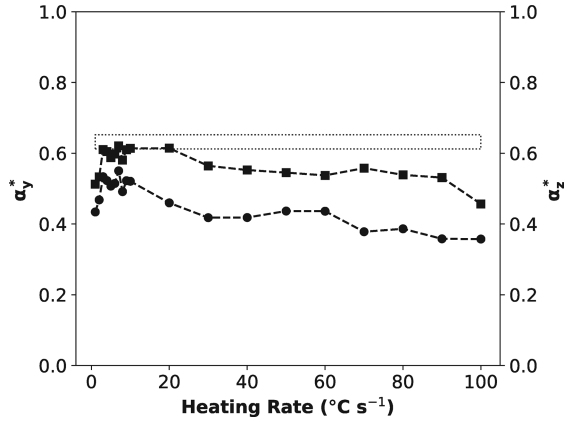

Figure 9. Maxima of the kinetic model functions $y(\alpha)$ (●) and $z(\alpha)$ (■) as a function of heating rate.

heating rates used. We note that both functions exhibit a dependence upon the heating rate, particularly between 100 °C s^{-1} and 10 °C s^{-1}, although for slower rates <10 °C s^{-1}, the dependence is weak. This validates the typical assumption that the rate of conversion is separable into a temperature dependent function and a model function that depends only on the extent of conversion α and not the heating rate β (eq 5).

$$\frac{d\alpha}{dT} = k(T)f(\alpha) \tag{5}$$

In Figure 10, a time−temperature-transformation diagram corresponding to the surfaces of constant conversion at 5% 25%,

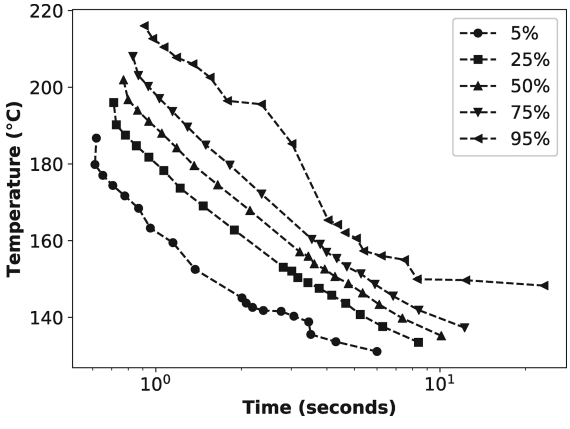

Figure 10. Time−temperature-transformation diagram corresponding to surfaces of constant conversion 5% (●), 25% (■), 50% (▲), 75% (▼) and 95% (◀).

50%, 75%, and 95% crystallinity is shown. Each plot represents an isocrystalline surface, where the data points correspond to the time and temperature required to reach a given value of the extent of conversion (Figure 5). This plot defines the heating conditions needed to obtain a given percent crystallinity.

There are some immediate implications of this data. First, precursors having endset decomposition temperatures that are lower than the crystallization temperatures shown on the TTT diagram can be used to convert into the oxide while preventing crystallite growth. Thus, we expect that zinc oxide films synthesized from solutions below 150 °C to be effectively amorphous, consisting of very small nuclei. This is consistent with reports elsewhere.[38]

It is interesting to compare these results to that of Rupp and co-workers, which, although chemically different, is expected to exhibit similar crystallization kinetics. The shape of the TTT diagram we obtain is similar to that obtained by Rupp and co-workers for CeO_2, except that here the time scales are much shorter and the temperatures much lower. However, we note that the CeO_2 and gadolinium alloyed $Ce_{0.8}Gd_{0.2}O_{1.9-x}$ films obtained by Rupp and co-workers had crystallites with sizes of 7 and 8 nm respectively as deposited at 400 °C. Thus, the growth of these crystallites likely occurs at faster rates and at lower temperatures, perhaps due to a reduced activation energy. Thus, the strength of using flash DSC is that the crystallization process and its rate dependence can be viewed in its entirety.

Practically, the information contained in the TTT diagram is suitable for rapid-thermal-annealing systems that are commercially available. However, since decomposition occurs at higher temperatures, it is necessary to combine with a rapid quenching process, which may not be feasible to the scale desired in a large-area process. On the basis of this data, at least two methods can be used to obtain amorphous metal-oxides from sol−gel precursors. First, precursors having endset decomposition temperatures that are lower than the onset temperatures of growth can be used to convert into the oxide while preventing crystallization. Second, the use of light to assist precursor decomposition (e.g., flash sintering) can be combined with mild heating (for mass diffusion) where the maximum temperature is restricted to be below that of the onset of growth as a means to produce amorphous oxide films for large-area electronics, optoelectronics, and thermoelectronics applications.

■ CONCLUSIONS

We have demonstrated a novel method to probe the kinetics of crystallite growth in sol−gel derived metal-oxide films *in situ*, using fast scanning nanocalorimetry. The success of this technique as a kinetic separations technique was demonstrated using zinc oxide derived from zinc acetate, a common sol−gel precursor used in the solution processing of zinc oxide films. Rapid heating and quenching enabled the controlled thermal decomposition of zinc acetate and nucleation of zinc oxide, leading to the observation of new and distinct exothermic peaks, associated with the growth of zinc oxide crystallites. These peaks were evaluated as the raw input to a kinetic model analysis used to quantify the growth kinetics including activation energy of crystallization and time−temperature-transformation diagram. This work is significant for several reasons. First, separating crystallization from decomposition in metal-oxide precursors is difficult due to large heats of formation, small activation energy of crystallization and high decomposition temperatures of sol−gel precursors. Second, the obtained TTT diagrams define the heating conditions needed to obtain a precise crystallinity and can therefore be used in defining processing protocols for sol−gel derived metal-oxide films. Third, the methods used are general and can be used to explore the growth kinetics in a wide variety of sol−gel derived metal-oxides based on other precursors (e.g., metal-halides, metal-nitrates). We note that, although this approach provides clear insight into the growth kinetics of the oxide phase originating within a precursor matrix, in actual sol−gel synthesis the growth kinetics is also influenced by additional interactions with solvents and additives/stabilizers

https://dx.doi.org/10.1021/acs.cgd.9b01339
Cryst. Growth Des. 2020, 20, 1590−1597

present in solution. Such effects may be investigated in future works.

■ ASSOCIATED CONTENT

Supporting Information

The Supporting Information is available free of charge at https://pubs.acs.org/doi/10.1021/acs.cgd.9b01339.

Supporting measurements for calorimetry experiments, including−total heat flow measured on each segment of the temperature−time profile applied during calorimetry experiments and Kissinger and Ozawa plots used to extract activation energies of crystallite growth (PDF)

■ AUTHOR INFORMATION

Corresponding Author

Andre Zeumault − *Department of Electrical Engineering and Computer Science and Department of Materials Science and Engineering, University of Tennessee, Knoxville, Tennessee, United States;* orcid.org/0000-0003-4629-9039; Phone: 865-974-5442; Email: azeumault@utk.edu

Author

Steven K. Volkman − *Department of Electrical Engineering and Computer Sciences, University of California, Berkeley, California, United States*

Complete contact information is available at: https://pubs.acs.org/10.1021/acs.cgd.9b01339

Notes

The authors declare no competing financial interest.

■ ACKNOWLEDGMENTS

We acknowledge the U.S. National Science Foundation for support through the DMREF program (DMR-1729737) and the EAGER program (DMR-1838276). We also acknowledge funding by the King Abdullah University of Science and Technology (KAUST) via a KAUST Competitive Research Grant (OSR-2016-CRG5-3029-01).

■ REFERENCES

(1) Subramanian, V.; Chang, J. B.; Vornbrock, A. d. l. F.; Huang, D. C.; Jagannathan, L.; Liao, F.; Mattis, B.; Molesa, S.; Redinger, D. R.; Soltman, D.; Volkman, S. K.; Zhang, Q. Printed electronics for low-cost electronic systems: Technology status and application development. ESSDERC 2008 - 38th European Solid-State Device Research Conference. Edinburgh, UK, 2008; pp 17−24.

(2) Calvert, P. Inkjet Printing for Materials and Devices. *Chem. Mater.* **2001**, *13*, 3299−3305.

(3) Mashayekhi, M.; Conde, A.; Ng, T. N.; Mei, P.; Ramon, E.; Martinez-Domingo, C.; Alcalde, A.; Teres, L.; Carrabina Bordoll, J. Inkjet Printing Design Rules Formalization and Improvement. *J. Disp. Technol.* **2015**, *11*, 658−665.

(4) Petti, L.; Münzenrieder, N.; Vogt, C.; Faber, H.; Büthe, L.; Cantarella, G.; Bottacchi, F.; Anthopoulos, T. D.; Tröster, G. Metal oxide semiconductor thin-film transistors for flexible electronics. *Appl. Phys. Rev.* **2016**, *3*, No. 021303.

(5) Yu, X.; Marks, T. J.; Facchetti, A. Metal oxides for optoelectronic applications. *Nat. Mater.* **2016**, *15*, 383−396.

(6) Ohta, H. *Metal Oxide-Based Thin Film Structures*; Elsevier, 2018; pp 441−464.

(7) Buchholz, D. B.; Ma, Q.; Alducin, D.; Ponce, A.; Jose-Yacaman, M.; Khanal, R.; Medvedeva, J. E.; Chang, R. P. H. The Structure and Properties of Amorphous Indium Oxide. *Chem. Mater.* **2014**, *26*, 5401−5411.

(8) Zeumault, A.; Scheideler, W.; Subramanian, V. Electrostatic Tuning of SprayDeposited ZnO for Controlled Mobility Enhancement. *Adv. Funct. Mater.* **2017**, *27*, 1701021.

(9) Tseng, Z.-L.; Kao, P.-C.; Chen, Y.-C.; Juang, Y.-D.; Kuo, Y.-M.; Chu, S.-Y. Effect of Thicknesses on the Structure, Conductivity, and Transparency of Al-doped ZnO Anodes in Organic Light-Emitting Diodes. *J. Electrochem. Soc.* **2011**, *158*, J310.

(10) Han, S.-Y.; Lee, D.-H.; Herman, G. S.; Chang, C.-H. Inkjet-Printed High Mobility Transparent−Oxide Semiconductors. *J. Disp. Technol.* **2009**, *5*, 520−524.

(11) Jang, J.; Kang, H.; Chakravarthula, H. C. N.; Subramanian, V. Fully Inkjet-Printed Transparent Oxide Thin Film Transistors Using a Fugitive Wettability Switch. *Adv. Electron. Mater.* **2015**, *1*, 1500086.

(12) Li, Y.; Lan, L.; Sun, S.; Lin, Z.; Gao, P.; Song, W.; Song, E.; Zhang, P.; Peng, J. All Inkjet-Printed Metal-Oxide Thin-Film Transistor Array with Good Stability and Uniformity Using Surface-Energy Patterns. *ACS Appl. Mater. Interfaces* **2017**, *9*, 8194−8200.

(13) Dasgupta, S.; Stoesser, G.; Schweikert, N.; Hahn, R.; Dehm, S.; Kruk, R.; Hahn, H. Printed and Electrochemically Gated, High-Mobility, Inorganic Oxide Nanoparticle FETs and Their Suitability for High-Frequency Applications. *Adv. Funct. Mater.* **2012**, *22*, 4909−4919.

(14) Lee, S.; Jeong, S.; Kim, D.; Park, B. K.; Moon, J. Fabrication of a solution-processed thin-film transistor using zinc oxide nanoparticles and zinc acetate. *Superlattices Microstruct.* **2007**, *42*, 361−368.

(15) Ellmer, K. In *Handbook of Transparent Conductors*; Ginley, D. S., Ed.; Springer US: Boston, MA, 2011; pp 193−263.

(16) Su, C.-Y.; Wang, C.-C.; Hsueh, Y.-C.; Gurylev, V.; Kei, C.-C.; Perng, T.-P. Enabling high solubility of ZnO in TiO_2 by nano-lamination of atomic layer deposition. *Nanoscale* **2015**, *7*, 19222−19230.

(17) Abdel-latief, A. Y.; Abdel-Rahim, M. A.; Shaalan, N. M.; Hamad, D. Structural and crystal growth kinetics studies for SnO_2 nanoparticles prepared via hydrothermal route. *Phase Transitions* **2017**, 1−15.

(18) Marinković, Z.; Mančić, L.; Miloševič, O. The nature of structural changes in nanocrystalline ZnO powders under linear heating conditions. *J. Eur. Ceram. Soc.* **2004**, *24*, 1929−1933.

(19) Srikanth, C. K.; Jeevanandam, P. Effect of anion on the homogeneous precipitation of precursors and their thermal decomposition to zinc oxide. *J. Alloys Compd.* **2009**, *486*, 677−684.

(20) Baker, P.; Sanderson, R.; Crouch, A. Sol−gel preparation and characterisation of mixed metal tin oxide thin films. *Thin Solid Films* **2007**, *515*, 6691−6697.

(21) Li, H.; Wang, J.; Liu, H.; Yang, C.; Xu, H.; Li, X.; Cui, H. Sol−gel preparation of transparent zinc oxide films with highly preferential crystal orientation. *Vacuum* **2004**, *77*, 57−62.

(22) Pokharel, J.; Shrestha, M.; Zhou, L.; Neto, V.; Fan, Q. Oriented Zinc Oxide Nanocrystalline Thin Films Grown from Sol-Gel Solution. *J. Coat. Sci. Technol.* **2015**, 46−50.

(23) Haya, S.; Brahmia, O.; Halimi, O.; Sebais, M.; Boudine, B. Sol−gel synthesis of Srdoped SnO_2 thin films and their photocatalytic properties. *Mater. Res. Express* **2017**, *4*, 106406.

(24) Misra, M.; Hwang, D.-K.; Kim, Y. C.; Myoung, J.-M.; Lee, T. I. Eco-friendly method of fabricating indium-tin-oxide thin films using pure aqueous sol-gel. *Ceram. Int.* **2018**, *44*, 2927−2933.

(25) Maddalena, A.; Dal Maschio, R.; Diré, S.; Raccanelli, A. Electrical conductivity of tin oxide films prepared by the sol-gel method. *J. Non-Cryst. Solids* **1990**, *121*, 365−369.

(26) Rupp, J. L. M.; Scherrer, B.; Schäuble, N.; Gauckler, L. J. Time-TemperatureTransformation (TTT) Diagrams for Crystallization of Metal Oxide Thin Films. *Adv. Funct. Mater.* **2010**, *20*, 2807−2814.

(27) Mukherjee, S.; Zhou, Z.; Schroers, J.; Johnson, W. L.; Rhim, W. K. Overheating threshold and its effect on time−temperature-transformation diagrams of zirconium based bulk metallic glasses. *Appl. Phys. Lett.* **2004**, *84*, 5010−5012.

(28) Johnson, E.; Kim, Y.-J.; Scott Chumbley, L.; Gleeson, B. Initial phase transformation diagram determination for the CD3MN cast duplex stainless steel. *Scr. Mater.* **2004**, *50*, 1351−1354.

(29) Rupp, J. L. M.; Scherrer, B.; Gauckler, L. J. Engineering disorder in precipitation-based nano-scaled metal oxide thin films. *Phys. Chem. Chem. Phys.* **2010**, *12*, 11114.
(30) Rupp, J. L. M.; Scherrer, B.; Harvey, A. S.; Gauckler, L. J. Crystallization and Grain Growth Kinetics for Precipitation-Based Ceramics: A Case Study on Amorphous Ceria Thin Films from Spray Pyrolysis. *Adv. Funct. Mater.* **2009**, *19*, 2790−2799.
(31) Poel, G. V.; Istrate, D.; Magon, A.; Mathot, V. Performance and calibration of the Flash DSC 1, a new, MEMS-based fast scanning calorimeter. *J. Therm. Anal. Calorim.* **2012**, *110*, 1533−1546.
(32) Eilers, P. H. C.; Boelens, H. F. Baseline Correction with Asymmetric Least Squares Smoothing. *Leiden University Medical Centre Report*, 2005.
(33) Vithal Ghule, A.; Lo, B.; Tzing, S.-H.; Ghule, K.; Chang, H.; Chien Ling, Y. Simultaneous thermogravimetric analysis and in situ thermo-Raman spectroscopic investigation of thermal decomposition of zinc acetate dihydrate forming zinc oxide nanoparticles. *Chem. Phys. Lett.* **2003**, *381*, 262−270.
(34) Málek, J. Kinetic analysis of crystallization processes in amorphous materials. *Thermochim. Acta* **2000**, *355*, 239−253.
(35) Friedman, H. L. Kinetics of thermal degradation of char-forming plastics from thermogravimetry. Application to a phenolic plastic. *J. Polym. Sci., Part C: Polym. Symp.* **1964**, *6*, 183−195.
(36) Ozawa, T. Applicability of Friedman plot. *J. Therm. Anal.* **1986**, *31*, 547−551.
(37) Málek, J. The applicability of Johnson-Mehl-Avrami model in the thermal analysis of the crystallization kinetics of glasses. *Thermochim. Acta* **1995**, *267*, 61−73.
(38) Tellier, J.; Kuščer, D.; Malič, B.; Cilenšek, J.; Škarabot, M.; Kovač, J.; Gonçalves, G.; Muševič, I.; Kosec, M. Transparent, amorphous and organics-free ZnO thin films produced by chemical solution deposition at 150°C. *Thin Solid Films* **2010**, *518*, 5134−5139.

https://dx.doi.org/10.1021/acs.cgd.9b01339
Cryst. Growth Des. 2020, 20, 1590−1597